Wave propagation and absorption simulations for helicon sources

Y. Mouzouris and J. E. Scharer
Department of Electrical and Computer Engineering, University of Wisconsin, Madison 53706

(Received 22 June 1998; accepted 16 September 1998)

A two-dimensional (2-D), finite-difference computer code is developed to examine helicon antenna coupling, wave propagation, collisionless Landau, and collisional heating mechanisms. The code calculates the electromagnetic wave fields and power absorption in an inhomogeneous, cold, collisional plasma. The current distribution of the launching antenna, which provides the full antenna spectra, is included in the model. An iterative solution that incorporates warm plasma thermal effects has been added to the code to examine the contribution of collisionless (Landau) wave absorption by electrons. Detailed studies of the wave fields and electron heating profiles at low magnetic fields ($B_0 < 100$ G), where both Trivelpiece–Gould (TG) and helicon (H) modes are present, are discussed. The effects of the applied uniform magnetic field ($B_0 = 10-1000$ G), 2-D (r,z) density profiles ($n_{e0} = 10^{11}-10^{13}$ cm^{-3}), neutral gas pressures of 1–10 mTorr and the antenna spectrum on collisional and collisionless wave field solutions and power absorption are investigated. Cases in which the primarily electrostatic (TG) surface wave dominates the heating and the power is absorbed near the edge region and cases in which the propagating helicon wave transports and deposits its energy in the core plasma region are examined. © *1998 American Institute of Physics.* [S1070-664X(98)04812-5]

I. INTRODUCTION

Helicon plasma sources are of considerable current interest for a variety of applications, including material surface modification, use as a high-density plasma source for neutral beam submicron etching of semiconductors, processing of flat panel displays, use as a large volume plasma source for space simulations, and for basic plasma source and wave propagation studies. Despite the substantial experimental interest in these sources,[1–8] no detailed two-dimensional (r,z) plasma profile wave simulations have been carried out to date to better model and understand propagation and absorption mechanisms. Several one-dimensional models that assume radially nonuniform plasma density and temperature profiles and axially uniform applied magnetic field and plasma density, have been presented in the literature.[9–13] Fischer *et al.*[9] examined helicon wave coupling and power absorption in a finite plasma column, assuming an axially uniform plasma and applied magnetic field. Their model includes temperature effects in the plasma dielectric tensor, which are necessary to model Landau damping. Kamenski and Borg[10] developed a one-dimensional magnetohydrodynamic numerical model, which is based on a finite-element method to analyze helicon wave coupling and the antenna radiation resistance for various antennas in a cylindrical, axially uniform, cold plasma. In a later paper,[11] they developed a one-dimensional cylindrical kinetic wave code, which includes the effects of collisional dissipation and Landau damping that are necessary for the description of wave absorption. Cho and Kwak[12] have investigated power absorption profiles using numerical integration methods for radially nonuniform helicon plasmas with finite axial lengths. Mouzouris and Scharer[13] developed the ANTENA2 simulation code, an improved version of the original ANTENA code[14] and suitable for describing helicon sources, to examine one-dimensional radial density and temperature profile effects on power absorption that include both collisional and collisionless damping mechanisms. In this work we extend previous studies by simultaneously including the effects of the axial, as well as radial, variation of the plasma density observed in experiments and an iterative solution incorporating Landau damping to the wave propagation and power absorption calculation, taking into account the full antenna spectra. The two-dimensional (r,z) wave field solutions, wave absorption, and electromagnetic Poynting flux flowing from the antenna to the plasma core for a realistic helicon source design are examined, utilizing graphics capabilities that we have also added to the cold plasma MAXEB code,[15] which include contour and surface plots.

The paper is organized as follows. In Sec. II we provide a brief analytic review of the propagating waves in the relevant plasma parameter range and their role in helicon plasma sources. A brief description of the physics and computational method of the modified MAXEB simulation code is presented in Sec. III. In Sec. IV, we discuss modeling results, which include benchmark test cases in which the electrostatic and electromagnetic limits of the helicon mode are examined, the effects of linear collisionless Landau and collisional damping on the two-dimensional spatial electron absorption, and a direct comparison with experimental data. In Sec. V we summarize the results.

II. DISPERSION RELATION OF WHISTLERS

The time harmonic form of Maxwell's equations, assuming there are no external currents, can be written as

$$\nabla \times \mathbf{E} = i\omega\mu_0 \mathbf{H}, \tag{1}$$

$$\nabla \times \mathbf{H} = -i\omega\epsilon_0 \overline{\mathbf{K}} \cdot \mathbf{E}, \tag{2}$$

where $\overline{\mathbf{K}}$ is the equivalent dielectric tensor as used in Stix,[16] which includes both plasma and displacement currents:

$$\overline{\mathbf{K}} = \begin{bmatrix} S & -iD & 0 \\ iD & S & 0 \\ 0 & 0 & P \end{bmatrix}. \tag{3}$$

After Fourier analysis in space, Maxwell's equations combine to give the homogeneous plasma wave equation in an unbounded plasma as

$$\mathbf{n} \times (\mathbf{n} \times \mathbf{E}) + \frac{\omega^2}{c^2} \overline{\mathbf{K}} \cdot \mathbf{E} = 0, \tag{4}$$

where $\mathbf{n} = \mathbf{k}c/\omega$ is the index of refraction vector whose direction is the direction of the wave vector $\mathbf{k}$ and whose magnitude is the index of refraction.

In order to obtain a nontrivial solution of the above vector wave equation, the determinant of the 3×3 matrix must be equal to zero. This condition yields the dispersion relation, which can be written in terms of the perpendicular refractive index $n_\perp = k_\perp c/\omega$,

$$An_\perp^4 - Bn_\perp^2 + C = 0, \tag{5}$$

where

$$A = S, \tag{6}$$

$$B = n_z^2[(S+P) - (RL+PS)], \tag{7}$$

$$C = P(n_z^2 - R)(n_z^2 - L). \tag{8}$$

The two solutions of the above equation are known as the fast [small $k_\perp$, high transverse phase velocity, helicon (H) mode] and slow (large $k_\perp$, slow transverse phase velocity, Trivelpiece–Gould (TG) mode].

Helicon waves are basically low-frequency ($\omega_{ci} \ll \omega \ll \omega_{ce} \ll \omega_{pe}$) bounded whistler waves (also known as R waves). In the ionosphere, whistler waves propagating parallel to the magnetic field are right-hand-circularly polarized electromagnetic waves. However, in a bounded system the waves can have an important electrostatic component and both right-hand and left-hand polarizations can occur.[17] The dispersion relation for R waves in a cold plasma can be written as follows:[16,18]

$$n^2 = \frac{c^2 k_t^2}{\omega^2} = 1 - \frac{\omega_{pe}^2}{\omega(\omega + i\nu - \omega_{ce}\cos\theta)}, \tag{9}$$

where $\cos\theta = k_z/k_t$, $k_t^2 = k_z^2 + k_\perp^2$. For the frequency range of interest, $\omega_{ci} \ll \omega \ll \omega_{ce} \ll \omega_{pe}$ the dispersion relation becomes

$$k_t^2 = \frac{\omega\omega_{pe}^2}{c^2(\omega_{ce}\cos\theta - \omega - i\nu)}, \tag{10}$$

which has two solutions for k_t,

$$k_t = \frac{\omega_{ce}k_z \pm \left(\omega_{ce}^2 k_z^2 - \dfrac{4\omega(\omega+i\nu)\omega_{pe}^2}{c^2}\right)^{1/2}}{2(\omega+i\nu)}. \tag{11}$$

The above equation shows that there are two values of $k_\perp$ for each k_z. These two modes are identified as the helicon (H) mode (minus sign) and the electrostatic Trivelpiece–Gould (TG) mode (positive sign).[19] When $\omega \ll \omega_{ce}$, only the helicon mode exists in a cold collisionless plasma and its dispersion relation can be simplified as

$$k_t^2 = \frac{\omega\omega_{pe}^2}{c^2\omega_{ce}\cos\theta}. \tag{12}$$

Solving the dispersion relation in terms of frequency, we obtain the following:[20]

(a) the helicon mode: $$\omega = \frac{\omega_{ce}k_z k_t c^2}{\omega_{pe}^2} - i\nu\frac{k_t^2 c^2}{\omega_{pe}^2}, \tag{13}$$

and

(b) the electrostatic TG mode: $$\omega = \omega_{ce}\frac{k_z}{k_t} - i\nu. \tag{14}$$

The low-frequency ($\omega \ll \omega_{ce}$) whistler in a bounded system is primarily an electromagnetic wave. As the frequency is increased up to and near the electron cyclotron frequency, ω_{ce}, the wave becomes more electrostatic in character and the Trivelpiece–Gould mode (bounded electron cyclotron wave) becomes the dominant mode.

III. INTRODUCTION TO THE TWO-DIMENSIONAL (r,z) SIMULATION CODE

Recent experimental observations[5,21–23] show that the plasma density for helicon plasma sources often peaks several wavelengths downstream from the antenna, and its axial variation can substantially affect the electromagnetic wave field profiles and power absorption of the plasma electrons. It is, therefore, necessary to develop a two-dimensional (r,z) model to account for the effects of the axial variation of the plasma density, temperature, and applied magnetic field on helicon wave propagation and absorption.

MAXEB, originally written by Whitson and Berry,[15] is a two-dimensional (r,z) simulation code that calculates the electromagnetic wave fields and power absorption in an inhomogeneous cold plasma immersed in a nonuniform magnetic field. The cylindrical magnetized plasma is surrounded by a radiofrequency (rf) inductive coil and both are enclosed in a metal conducting tube. The electromagnetic fields are determined by solving the time-harmonic form of Maxwell's equations,

$$\nabla \times \mathbf{E} = i\omega\mu_0 \mathbf{H}, \tag{15}$$

$$\nabla \times \mathbf{H} = -i\omega\epsilon_0 \overline{\mathbf{K}} \cdot \mathbf{E} + \mathbf{J}_{\text{ext}}, \tag{16}$$

where

$$\overline{\mathbf{K}} = \begin{bmatrix} k_{11} & k_{12} & k_{13} \\ k_{21} & k_{22} & k_{23} \\ k_{31} & k_{32} & k_{33} \end{bmatrix} \tag{17}$$

is the dielectric tensor and $\mathbf{J}_{\text{ext}}$ is the external antenna current density. In the cold plasma limit, the $\mathbf{K}$ tensor reduces to the familiar plasma equivalent dielectric tensor used in Stix[16] and the tensor elements attain the values,

$$k_{11}=k_{22}=S, \quad k_{33}=P, \quad k_{12}=-k_{21}=-iD, \qquad k_{13}=k_{23}=k_{31}=k_{32}=0. \tag{18}$$

The code is written for a general orthogonal curvilinear coordinate system (u_1,u_2,u_3), but for the purpose of this paper cylindrical coordinates are used. MAXEB assumes axisymmetry and Fourier analyses in the azimuthal direction to reduce the three-dimensional boundary-value problem to two dimensions: u_1 and u_3, or in cylindrical coordinates, the radial (r) and axial (z) direction, respectively. The fields can be then decomposed as follows:

$$[\mathbf{E},\mathbf{H}]=\sum_{m=-\infty}^{m=+\infty}[\mathbf{E},\mathbf{H}(u_1,u_3)]e^{imu_2}. \tag{19}$$

The components of Maxwell's equations form a set of equations that can express the perpendicular components of the electric and magnetic fields, $\mathbf{E}_\perp$, $\mathbf{H}_\perp$, in terms of the third component (E_2,H_2) and its derivatives. The set of equations needed to solve for the E_2 and H_2 components is determined from the original curl equations. Applying Stoke's theorem to the integral form of the field equations yields

$$\int_S(\nabla\times\mathbf{E})\cdot\mathbf{dS}=\oint_c\mathbf{E}\cdot d\mathbf{r}=i\omega\int_S\mathbf{B}\cdot d\mathbf{S}, \tag{20}$$

$$\int_S(\nabla\times\mathbf{B})\cdot d\mathbf{S}=\oint_c\mathbf{B}\cdot d\mathbf{r}=\int_S(\mathbf{J}_{\text{ext}}-i\omega\epsilon_0\overline{\mathbf{K}}\cdot\mathbf{E})\cdot d\mathbf{S}, \tag{21}$$

where $d\mathbf{S}$ is chosen to be in the (u_1,u_3) surface and $d\mathbf{r}=\Sigma_{j=1}^{3}h_j du_j\mathbf{e_j}$ with $\mathbf{e_j}$ being the unit tangent vectors to the (u_1,u_2,u_3) curves. We can then write the above equations as

$$\frac{1}{i\omega}\oint_c\mathbf{E}_\perp\cdot(h_1du_1\mathbf{e_1}+h_3du_3\mathbf{e_3})=|\mathbf{n}|\int_S B_2dS =|\mathbf{n}|\int_S h_2B_2\frac{dS}{h_2}=|\mathbf{n}|\int_S i\chi\frac{dS}{h_2} \tag{22}$$

and

$$\frac{1}{i\omega}\oint_c\mathbf{B}_\perp\cdot(h_1du_1\mathbf{e_1}+h_3du_3\mathbf{e_3}) =|\mathbf{n}|\int_S\left(\mathbf{J}_2-\mathbf{K}_{\perp 2}\cdot\mathbf{E}_\perp-\frac{k_{22}}{h_2}(h_2E_2)\right)dS =|\mathbf{n}|\int_S\left(\mathbf{J}_2-\mathbf{K}_{\perp\mathbf{2}}\cdot\mathbf{E}_\perp-i\lambda\frac{k_{22}}{h_2}\right)dS,$$

where $|\mathbf{n}|=|\mathbf{e_2}\cdot\mathbf{e_1}\times\mathbf{e_3}|$, $\mathbf{K}_{\perp\mathbf{2}}=[k_{21}k_{23}]$, and the components E_2 and H_2 are replaced with the scalar potentials $E_2h_2=i\lambda$ and $B_2h_2=i\chi$.

These equations form a coupled set in (χ,λ) and can be written in the following form:

$$\oint_c h_1E_1du_1+h_3E_3du_3=-|\mathbf{n}|\omega\int_S\chi\frac{h_1h_3}{h_2}du_1du_3 \tag{23}$$

and

$$\oint_c h_1B_1du_1+h_3B_3du_3 =i\omega|\mathbf{n}|\int_S\left(j_2-k_{21}E_1-k_{23}E_3-\frac{k_{22}}{h_2}i\lambda\right)h_1h_3du_1du_3. \tag{24}$$

Note that for the cylindrical coordinate system, the scale factors attain the values $h_1=1$, $h_2=r$, and $h_3=1$. The integrals are then approximated on a two-dimensional (u_1,u_3) grid. The right-hand side of the above equations is evaluated at the center of each enclosed path used to compute the left-hand side. Since every quantity can be determined in terms of χ and λ and their derivatives, the above equations, along with boundary conditions, form a set of equations appropriate for a numerical solution. We have added the faster MA42 matrix solver package,[24] which is used to obtain the solution of this set of equations, which reduces to the general form:

$$\mathbf{Ax}=\mathbf{b}, \tag{25}$$

where the matrix $\mathbf{A}$ is large and sparse and is not assumed to be symmetric or of any particular structure.

The current distribution of the launching antenna, which provides the full antenna spectra, is included in the model. The external driving currents are assumed to be given as a function of (r,z). The particle conserving Krook model[25] is implemented to treat collisional damping.

Several antenna configurations, including the Nagoya-type III and $m=0$ coils, can be modeled with MAXEB. Sheath effects are not important for these sources, since the sheath thickness is very thin (of the order of 10 microns for typical parameters of $T_e=3$ eV and $n_e=10^{12}$ cm^{-3}), and the sheath velocity $(v_s=\sqrt{T_e/m_i})$ is much slower than the electron thermal velocity, which preserves quasineutrality.

We have modified the code to include local thermal effects. The local linear Landau damping term is treated by computing a local k_z value using the electromagnetic wave fields previously calculated by the code. In particular, the parallel wave number can be determined and written as:

$$k_z=\frac{\partial\phi}{\partial z}, \tag{26}$$

where ϕ is the phase of the axial electric field, E_z, the component of the electric field responsible for the Landau damping effect. A four-point central differencing scheme,[26] which has an order of accuracy of $(\Delta z)^4$, is used when calculating the derivative of the phase with respect to the axial position z. These k_z values are used to evaluate the kinetic form of the dielectric element P of the plasma dielectric tensor. The warm plasma dielectric tensor, $\overline{\mathbf{K}}_{\text{warm}}$ with the P component now given by

$$P=1-\sum_{\alpha}\ \frac{\omega_{p\alpha}^2}{(k_z v_\alpha)^2}\frac{Z'(\zeta_n)}{\left(1+\dfrac{i\nu_\alpha}{k_z v_\alpha}Z(\zeta_n)\right)}, \tag{27}$$

is then used along with the Maxwell's equations to determine the new electromagnetic fields corrected for local thermal effects. The appropriate collision frequency ν_{eff} for the Krook model is given by

$$\nu_{\text{eff}}=\nu_{en}+\nu_{ei}, \tag{28}$$

where $\nu_{en}=n_n<\sigma v_{\text{the}}>$, and $\nu_{ei}=2.9\times10^{-6}\times[n_e(\text{cm}^{-3})\ \ln\Lambda/T_{eV}^{3/2}]$ are collision frequencies for electron–neutral and electron–ion collisions, respectively, and depend on the density and temperature (r,z) profiles. The electron–argon collision cross section that is weakly dependent on temperature is given by $\sigma=5\times10^{-15}$ cm^2 and the neutral density is $n_n=3.54\times10^{13}$ p(mTorr) cm^{-3}. The argument ζ_n used in Eq. (26) is defined as

$$\zeta_n=\frac{\omega+i\nu_\alpha+n\omega_{e\alpha}}{k_z v_\alpha}, \tag{29}$$

where α is the species type (electrons, ions) and Z is the plasma dispersion function tabulated by Fried and Conte,[27]

$$Z(\zeta)=\frac{1}{\sqrt{\pi}}\int_{\infty}^{\infty}dz\ \frac{e^{-z^2}}{z-\zeta},\quad \text{Im}\ \zeta>0. \tag{30}$$

For this paper, we neglect the effect of cyclotron damping on helicon waves, which is negligible in most helicon sources that operate sufficiently far from electron cyclotron resonance. The argument ζ_n can then be reduced to $\zeta_0=(\omega+i\nu_\alpha)/k_z v_\alpha$ for the case $n=0$.

The previously calculated k_z values are recalculated and checked utilizing the new wave fields, following the same procedure described above. The power absorbed by the plasma electrons due to Landau and collisional damping of the helicon wave is then given by

$$P=\frac{1}{2}\ \text{Re}(\mathbf{E}\cdot\mathbf{J}_{\mathbf{p}}^{*})=\frac{\omega\epsilon_0}{2}\ \mathbf{E}^{*}\cdot\overline{\mathbf{K}}_{\text{warm}}^{(\mathbf{a})}\cdot\mathbf{E}. \tag{31}$$

The iterative procedure converges rapidly (it needs just one to two iterations for the change in the wave field values to be less than 15%) for the collisional cases, where ν/ω is greater than 0.2. At lower gas pressures, $p<1$ mTorr, a convergent solution is reached after 10–15 iterations.

IV. MODELING RESULTS

The modified MAXEB computer code is used to model and study helicon plasma sources. We benchmarked the modified MAXEB code with our ANTENA2 code for an axially uniform plasma in a uniform axial magnetic field. In particular, the radial electric and magnetic wave fields and the radial power absorption profile obtained by MAXEB for an axially uniform density profile are in very good agreement with those obtained by ANTENA2, as shown in Figs. 1–3. We examine wave propagation (axial and radial wave field components) and electron heating due to linear collisional and collisionless wave absorption mechanisms for given two-dimensional (r,z) plasma density and temperature profiles taken from experimental data. A typical run using a grid size of 50×120 in the radial and axial position, respectively, for a cylindrical plasma column of length $L=120$ cm and radius $r=5$ cm and utilizing only the dominant azimuthal $m=+1$ mode requires about five minutes of run time on our Sun Ultra2 model 2300 workstation.

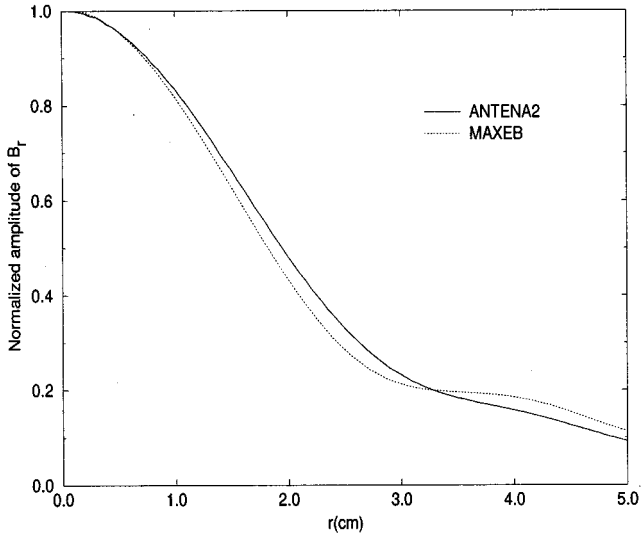

FIG. 1. The normalized radial profiles of the B_r field in plasma computed 15 cm away from the antenna for the $m=+1$ mode, $B_0=150$ G, $n_{e0}=2\times10^{12}$ cm^{-3}, $f=13.56$ MHz obtained from ANTENA2 (solid line) and MAXEB (dotted line).

Both the helicon (H) and the electrostatic (TG) modes exist at low magnetic fields and the structure of these modes was simulated using the MAXEB and ANTENA2 computer

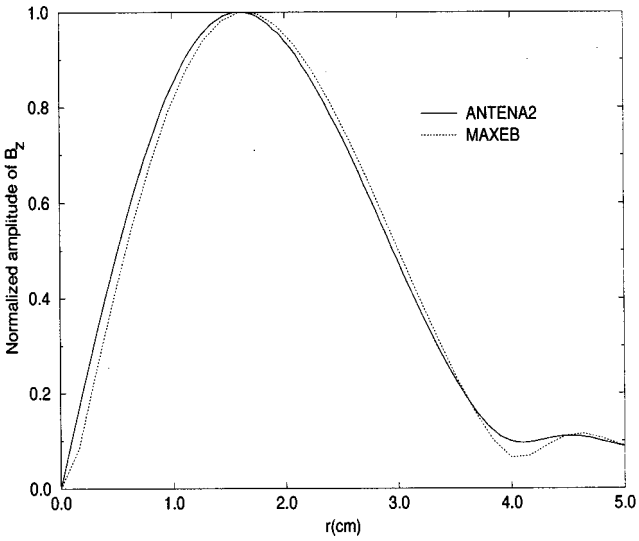

FIG. 2. The normalized radial profiles of the B_z field in plasma computed 15 cm away from the antenna for the $m=+1$ mode, $B_0=150$ G, $n_{e0}=2\times10^{12}$ cm^{-3}, $f=13.56$ MHz obtained from ANTENA2 (solid line) and MAXEB (dotted line).

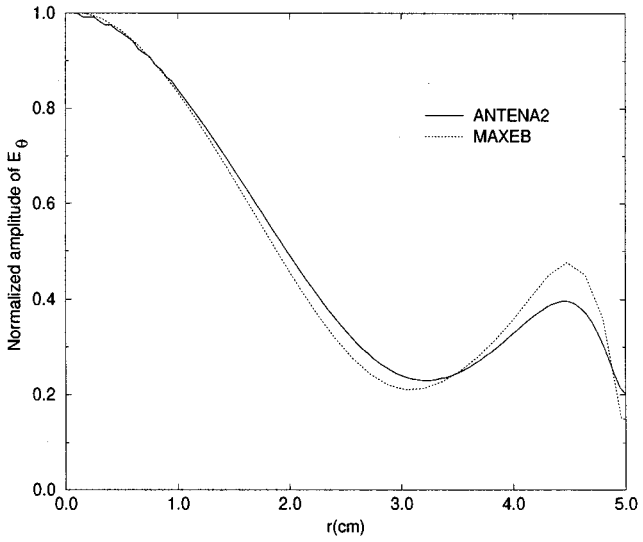

FIG. 3. The normalized radial profiles of the E_θ field in plasma computed 15 cm away from the antenna for the $m=+1$ mode, $B_0=150$ G, $n_{e0}=2\times10^{12}$ cm^{-3}, $f=13.56$ MHz obtained from ANTENA2 (solid line) and MAXEB (dotted line).

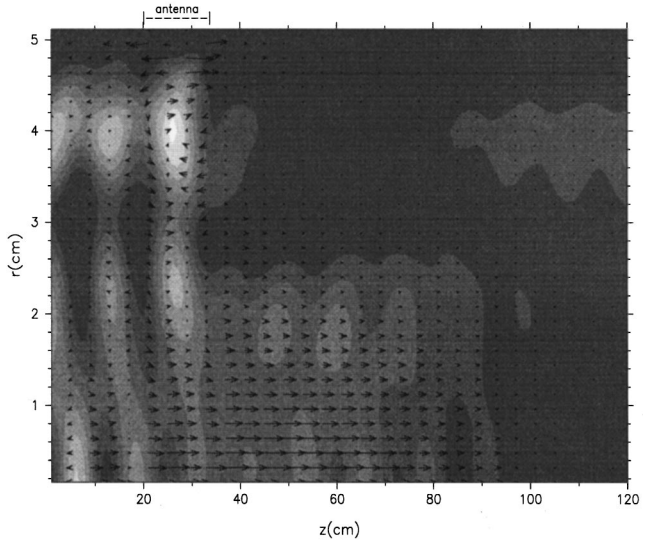

FIG. 5. Power flow and power absorbed [$\max(P_{abs})=0.60$ W/cm^3] by the electrons due to collisional damping of the TG and H waves for the $m=+1$ mode, $B_0=80$ G, $n_{e0}=5\times10^{11}$ cm^{-3}, $f=13.56$ MHz, $p=1$ mTorr.

codes. The following table presents the parameter ranges examined and simulated using these codes:

$B_0=20-1000$ G, $f=13.56$ MHz,
$T_e=3$ eV, $r_{\text{plasma}}=5$ cm,
$n_{e0}=10^{11}-10^{13}$ cm^{-3},
$\nu_{\text{eff}}/\omega=0.1-0.6$.

Figures 4–7 illustrate the Poynting vector and power absorbed by the electrons for the dominant $m=+1$ azimuthal mode number for different values of the applied magnetic field. The arrows describe the direction of the Poynting vector and their length represents the magnitude of the Poynting vector. The linear contour plots illustrate the spatial profiles of the absorbed power with the lightest shade shown in white, indicating the strongest absorption zones and the darkest indicating the lowest absorption zones. The maximum value of the absorbed power is given in each figure to provide a better interpretation of the plots. The dark zones correspond to the smallest power absorption.

The plasma density profile, which has a peak amplitude of $n_{e0}=5\times10^{11}$ cm^{-3}, is assumed to be parabolic in the radial direction and uniform in the axial direction. The electron temperature profile is assumed to be uniform throughout the plasma column, with an amplitude of $T_e=3$ eV. Cases corresponding to an experimentally relevant axially varying

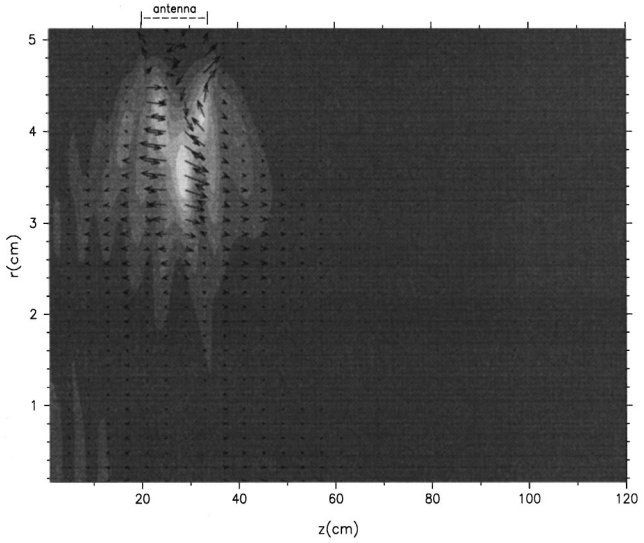

FIG. 4. Power flow and power absorbed [$\max(P_{abs})=1.3$ W/cm^3] by the electrons due to collisional damping of the TG and H waves for the $m=+1$ mode, $B_0=20$ G, $n_{e0}=5\times10^{11}$ cm^{-3}, $f=13.56$ MHz, $p=1$ mTorr.

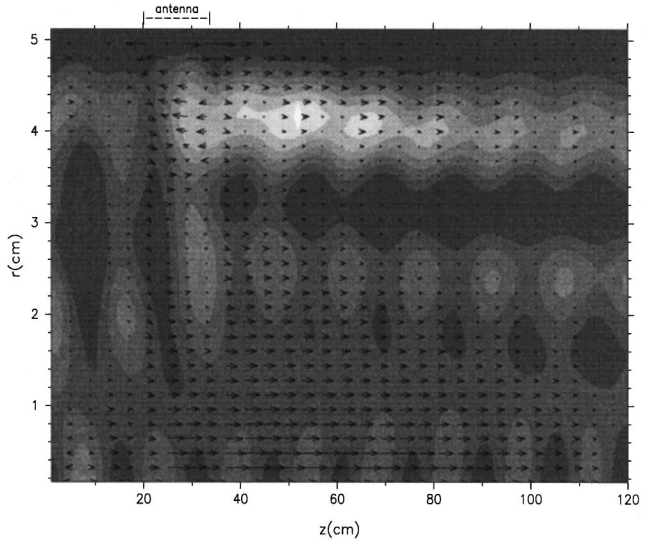

FIG. 6. Power flow and power absorbed [$\max(P_{abs})=0.45$ W/cm^3] by the electrons due to collisional damping of the TG and H waves for the $m=+1$ mode, $B_0=110$ G, $n_{e0}=5\times10^{11}$ cm^{-3}, $f=13.56$ MHz, $p=1$ mTorr.

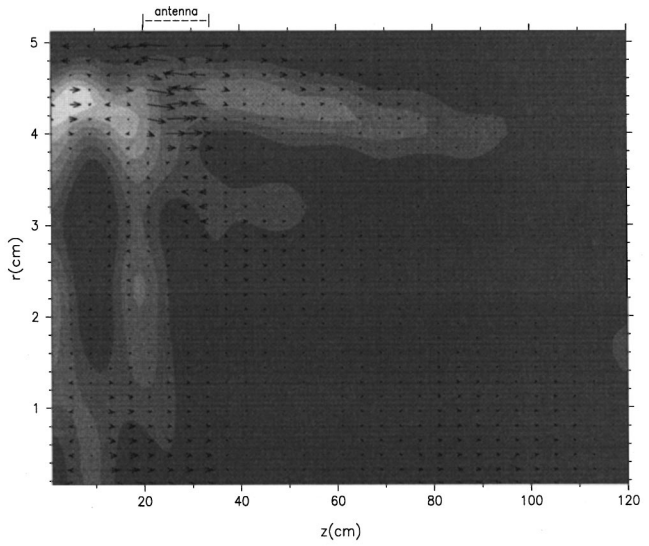

FIG. 7. Power flow and power absorbed $[\max(P_{\text{abs}})=1.0\ \text{W/cm}^3]$ by the electrons due to collisional damping of the TG and H waves for the $m=+1$ mode, $B_0=150$ G, $n_{e0}=5\times10^{11}\ \text{cm}^{-3}$, $f=13.56$ MHz, $p=1$ mTorr.

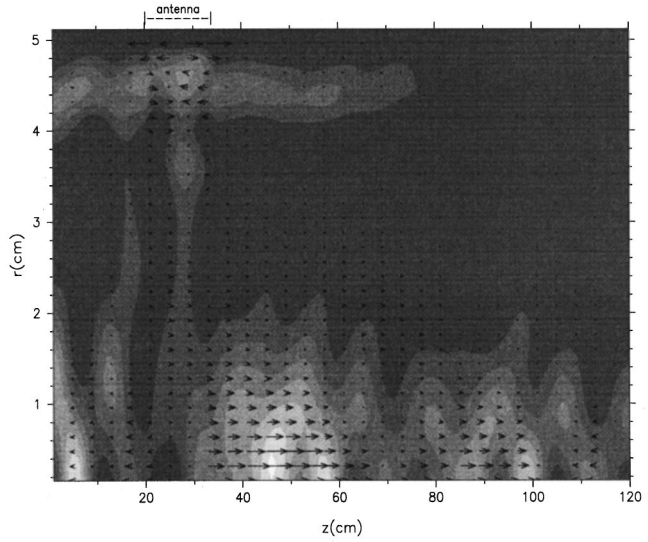

FIG. 8. Power flow and power absorbed $[\max(P_{\text{abs}})=1.1\ \text{W/cm}^3]$ by the electrons due to collisional damping of the TG and H waves for the $m=+1$ mode, $B_0=150$ G, $n_{e0}=2\times10^{12}\ \text{cm}^{-3}$, $f=13.56$ MHz, $p=1$ mTorr.

density profile are discussed later. The total coupled power is kept constant ($P_{\text{RF}}=1000$ W) for the simulations by adjusting the current on the antenna according to the value of the antenna radiation resistance computed by the code. The code is a linear absorption code that does not treat ionization, recombination, nor plasma losses, and changes in assumed plasma densities for the same pressure and magnetic fields would be obtained by variations in coupled power in the experimental case. The gas is argon with a neutral pressure ranging from 1 to 10 mTorr, which corresponds to $\nu_{en}/\omega=0.1-1$ at an electron temperature of 3 eV. For a plasma density of $n_{e0}=5\times10^{11}\ \text{cm}^{-3}$ and gas pressure of 1 mTorr, the electron–neutral collision frequency is much higher than the electron–ion collision frequency. The modeling parameters chosen are typical for these sources.

The modeled cylindrical plasma column is 120 cm long, 10 cm in diameter, and is surrounded by a conducting wall of radius $r=8.0$ cm. The conducting endplates, as modeled in MAXEB, are located at the axial positions $z=0$ cm and $z=120$ cm. A Nagoya type-III antenna of length $l=15$ cm and radius $r=5.0$ cm is centered at $z=27.5$ cm.

Figure 4 shows that at a low magnetic field ($B_0=20$ G) and an Ar pressure of 1 mTorr, the absorbed power is localized near the antenna and the coupling is dominated by the Trivelpiece–Gould mode, which propagates near the outer plasma edge region.

Figures 5 and 6 show that at higher magnetic fields ($B_0=80$, 110 G) the coupling is dominated by the propagating helicon mode that transports and deposits the coupled power well away from the antenna region. The electrostatic TG mode is strongly damped and thus deposits power near the edge of the plasma. However, for a magnetic field of $B_0=150$ G, as illustrated in Fig. 7, the axial wave number, k_z, excited by the Nagoya type-III antenna and plasma parameters assumed, does not satisfy the dispersion relation of Eq. (13) obtained in Sec. II for the $m=+1$ helicon mode. As a result, the propagating helicon mode is not excited and the power is deposited entirely near the edge by the antenna.

The power transferred to the plasma can be computed from the wave fields as

$$P_c=-\frac{1}{2}\int \mathbf{E}\cdot\mathbf{J}^*_{\text{ant}}d\mathbf{V}. \tag{32}$$

The load impedance of the antenna is then written as

$$Z=\frac{2P_c(w)}{|I|^2}=R_A+jX_A, \tag{33}$$

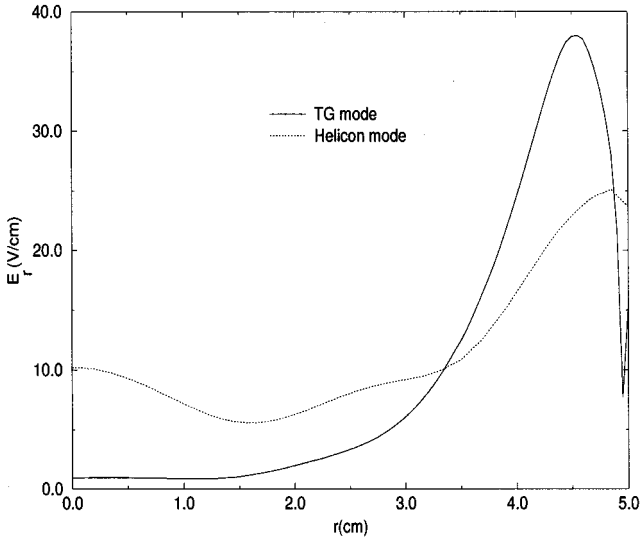

FIG. 9. The radial profile of the E_r field for the TG (solid line) and helicon (dotted line) mode obtained from ANTENA2 15 cm away from the antenna for the $m=+1$ mode, $B_0=150$ G, $n_{e0}=2\times10^{12}\ \text{cm}^{-3}$, $f=13.56$ MHz.

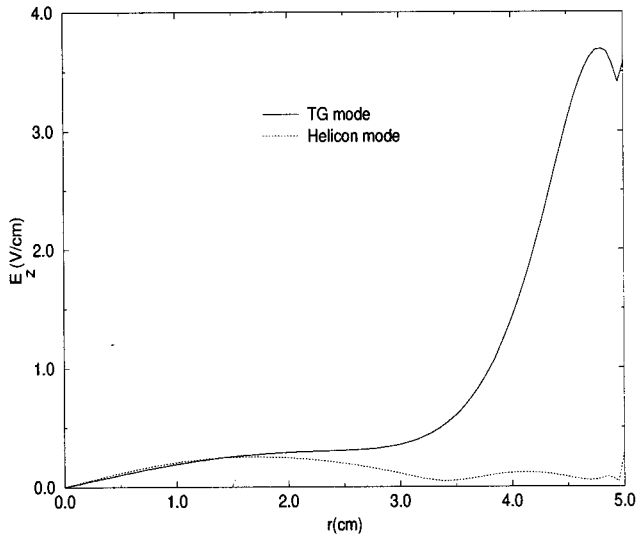

FIG. 10. The radial profile of the E_z field for the TG (solid line) and helicon (dotted line) mode obtained from ANTENA2 15 cm away from the antenna for the $m=+1$ mode, $B_0=150$ G, $n_{e0}=2\times10^{12}$ cm^{-3}, $f=13.56$ MHz.

where $R_A=R_r+R_L=$antenna resistance, $R_r=$radiation resistance of the antenna, $R_L=$skin loss resistance of the antenna, and $X_A=$antenna reactance.

The radiated power input to the plasma is proportional to $|I|^2R_r/2$, whereas the reactive power stored in the fields is represented by the reactive part of the impedance. The antenna impedance obtained for the $B_0=150$ G case is $Z=0.29+j5.15\,\Omega$ and has a much lower radiation resistance than the one obtained for $B_0=110$ G, which has a value of $Z=0.61+j5.25\,\Omega$. The higher value of the radiation resistance for the $B_0=110$ G case is due to the excitation of the helicon mode. Clearly, the power input to the plasma for a given current can be increased by maximizing the radiation resistance and this was achieved for the parameters corresponding to Fig. 6 with an applied magnetic field of $B_0=110$ G.

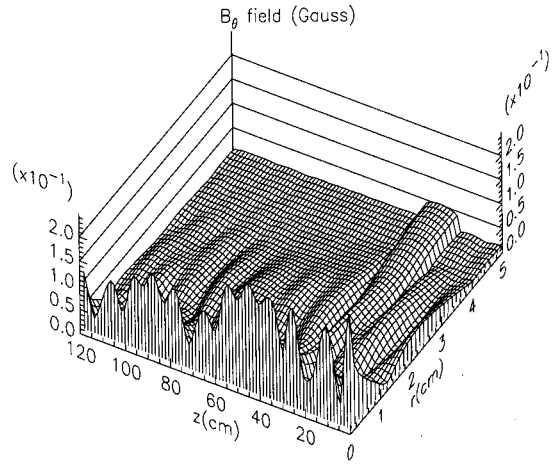

FIG. 12. Radial and axial variation of the B_θ field for the $m=+1$ mode, $B_0=150$ G, $n_{e0}=2\times10^{12}$ cm^{-3}, $f=13.56$ MHz.

Figure 8 illustrates the power flow and power absorbed by the electrons due to collisional damping of both the helicon (H) and Trivelpiece–Gould (TG) mode. The parameters chosen are: $B_0=150$ G, $n_{e0}=2\times10^{12}$ cm^{-3}, and a gas pressure of 1 mTorr. The ANTENA2 code is used to illustrate the existence of both modes, since MAXEB solves for the total wave field solution and cannot separate the two modes. Figures 9 and 10 obtained using our ANTENA2 code show that the amplitude of the radial E_r and axial E_z wave fields of the TG mode that peak near the edge are much higher than the corresponding fields of the helicon mode. The contribution of the TG mode to the total absorbed power is significant and dominates the heating process near the surface of the plasma column. In contrast, the propagating helicon mode carries and deposits the power through collisional damping away from the antenna region. The radial magnetic wave fields, B_r, B_θ, and B_z obtained by MAXEB and shown in Figs. 11, 12, and 13 confirm the existence of the $m=+1$ helicon mode[17] and are in good agreement with experimental results.[28]

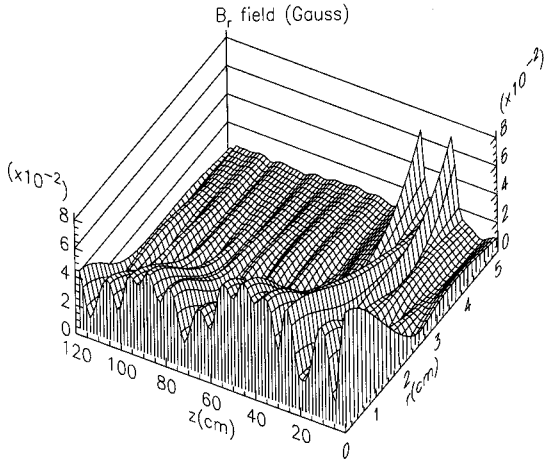

FIG. 11. Radial and axial variation of the B_r field for the $m=+1$ mode, $B_0=150$ G, $n_{e0}=2\times10^{12}$ cm^{-3}, $f=13.56$ MHz.

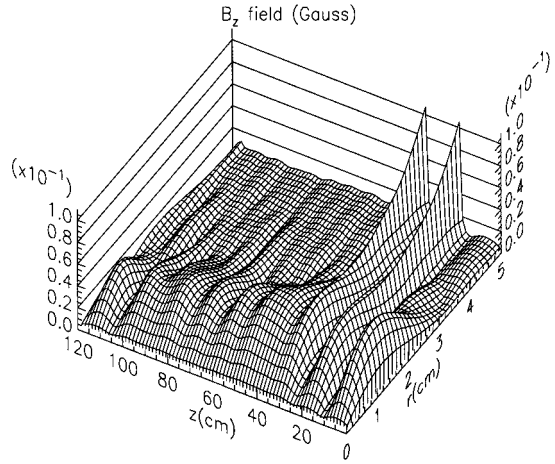

FIG. 13. Radial and axial variation of the B_z field for the $m=+1$ mode, $B_0=150$ G, $n_{e0}=2\times10^{12}$ cm^{-3}, $f=13.56$ MHz.

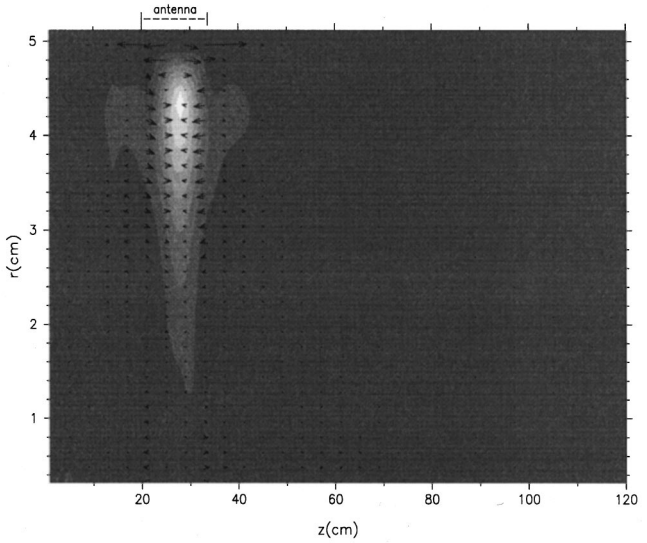

FIG. 14. Power flow and power absorbed [$\max(P_{abs})=1.8\ \mathrm{W/cm^3}$] by the electrons due to collisionless Landau and collisional damping of the TG and H waves for the m=+1 mode and $B_0=110$ G, $n_{e0}=2\times10^{12}\ \mathrm{cm^{-3}}$, $f=13.56$ MHz, $p=5$ mTorr.

Studies using the new, warm plasma, K_{33} term of the dielectric tensor show that collisional damping (by electron–neutral collisions) is the dominant heating mechanism for gas pressures greater than 2 mTorr and higher densities ($>2\times10^{12}\ \mathrm{cm^{-3}}$). Figure 14 illustrates the power absorbed by the electrons at a magnetic field $B_0=110$ G and gas pressure of 5 mTorr. Landau damping on the 3 eV Maxwellian background is found to be negligible for this case and the power is absorbed entirely through collisional damping of the wave as it propagates away from the antenna. At lower pressures ($p=1$ mTorr), as shown in Fig. 15 when compared to Fig. 6, Landau damping becomes important and is incorporated in the calculation of the power absorbed by the

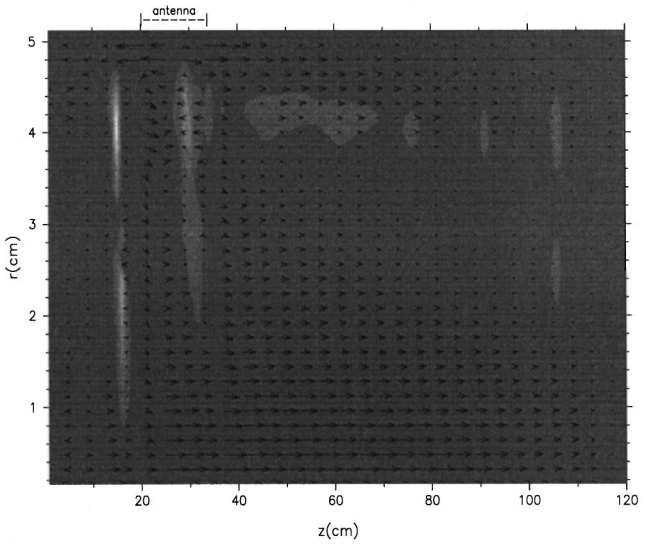

FIG. 15. Power flow and power absorbed [$\max(P_{abs})=2.3\ \mathrm{W/cm^3}$] by the electrons due to collisionless Landau and collisional damping of the TG and H waves for the $m=+1$ mode and $B_0=110$ G, $n_{e0}=5\times10^{11}\ \mathrm{cm^{-3}}$, $f=13.56$ MHz, $p=1$ mTorr.

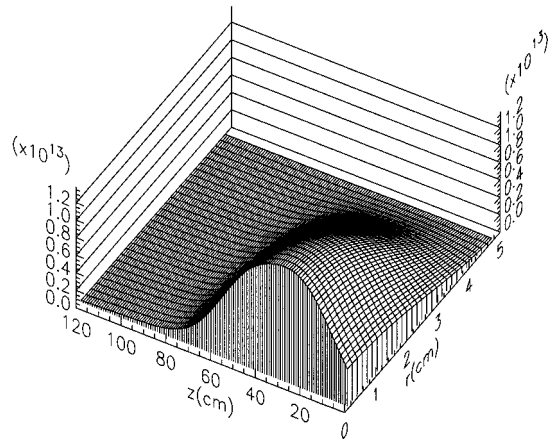

FIG. 16. Plasma density profile.

electrons. Collisionless Landau damping heats the electrons mainly at the surface where the plasma density is low and the resonant electrons have velocities near the wave phase velocity determined by $v_{ph}=\omega/k_z$. The ratio of the parallel phase to thermal velocity, v_{ph}/v_{th}, attains a value of about 1, where the Landau damping process is most effective.

A helicon experimental cylindrical plasma recently developed in our research group[28] is 120 cm long, 10 cm in diameter with conducting endplates located at the axial positions $z=0$ cm and $z=120$ cm. A Nagoya type-III antenna of length $l=15$ cm and radius $r=5.0$ cm is centered at $z=27.5$ cm. The measured plasma density and applied magnetic field profiles shown in Figs. 16 and 17 are used as an input to MAXEB, which utilizes the local plasma dielectric tensor for the calculation of the wave fields and the electron heating profile. Figure 18 illustrates the Poynting vector and absorbed power by the electrons for a localized wave model utilizing the experimentally obtained, axially varying plasma density profile. The electron heating profile for this case differs considerably from the one computed for an axially uniform plasma, as shown in Fig. 19. The axial inhomogeneities in the plasma density cause distributed reflections and prevent the wave from propagating to the far end of the plasma chamber. The steep density gradient near the axial position

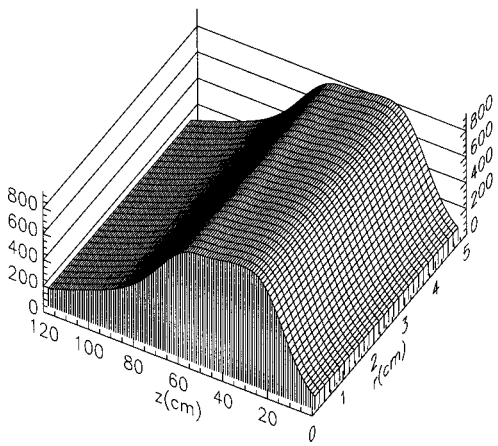

FIG. 17. Applied magnetic field profile.

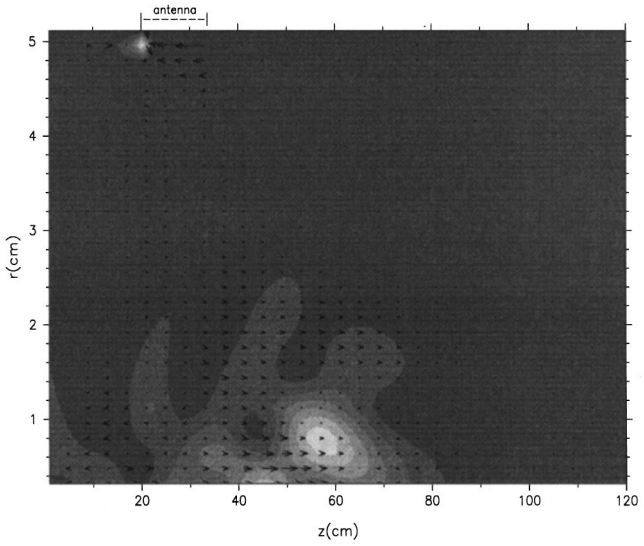

FIG. 18. Power flow and power absorbed $[\max(P_{abs})=2.2\ \mathrm{W/cm^3}]$ by the electrons for the experimentally obtained plasma density profile.

$z=70$ cm causes the propagating helicon wave to substantially reflect and thus deposit its wave energy near the antenna region.

V. SUMMARY AND CONCLUSIONS

A two-dimensional (r,z) computer code is used to study and model helicon sources. Detailed studies of the wave fields and electron heating profiles at low magnetic fields $(B_0<150\ \mathrm{G})$ were discussed. We have demonstrated that the primarily electrostatic TG mode dominates the heating at low magnetic fields and deposits its wave energy near the edge region. At higher magnetic fields $(B_0>80\ \mathrm{G})$, the propagating helicon mode transports and deposits its energy in the core plasma region away from the antenna. The code was modified to include warm plasma thermal effects and the contribution of linear collisionless (Landau) wave absorption by electrons. We have found that collisional damping is the dominant heating mechanism for moderate pressures ($p>2$ mTorr) and higher densities ($n_e>2\times10^{12}\ \mathrm{cm^{-3}}$). However, at low pressure ($p<2$ mTorr) Landau damping becomes important and heats the electrons mainly at the surface, where the resonant electrons have velocities near the wave phase velocity. The axial variation of the plasma density profile, as measured in experiments, can substantially affect the electromagnetic wave field and electron heating profiles. A future paper will examine the effects of strong magnetic field inhomogeneities and comparison with experimental measurements.

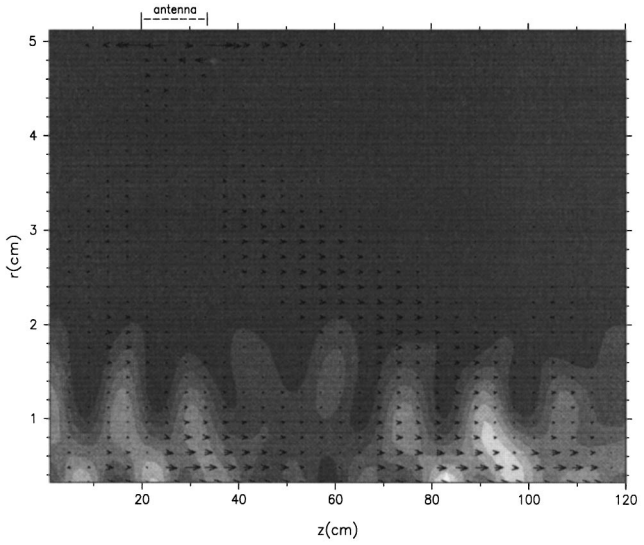

FIG. 19. Power flow and power absorbed $[\max(P_{abs})=1.4\ \mathrm{W/cm^3}]$ by the electrons for an axially uniform plasma density and magnetic field profile.

ACKNOWLEDGMENTS

The authors would like to thank L. Berry and J. Whitson for providing a copy of their computer code MAXEB, along with their helpful comments and suggestions. We are also grateful to M. Bettenhausen for many valuable discussions.

This work was supported by National Science Foundation Grant No. ECS-9632377.

[1] R. W. Boswell, Plasma Phys. Controlled Fusion **26**, 1147 (1984).
[2] A. Komori, T. Shoji, K. Miyamoto, J. Kawai, and K. Kawai, Phys. Fluids B **3**, 893 (1991).
[3] F. F. Chen, J. Vac. Sci. Technol. A **10**, 1389 (1992).
[4] T. Shoji, Y. Sakawa, S. Nakazawa, K. Kadota, and T. Sato, Plasma Sources Sci. Technol. **2**, 5 (1993).
[5] A. R. Ellingboe and R. W. Boswell, Phys. Plasmas **3**, 2797 (1996).
[6] A. W. Molvik, A. R. Ellingboe, and T. D. Ronglien, Phys. Rev. Lett. **79**, 233 (1997).
[7] P. A. Keiter, E. E. Scime, and M. M. Balkey, Phys. Plasmas **4**, 2741 (1997).
[8] R. T. S. Chen and N. Hershkowitz, Phys. Rev. Lett. **80**, 4677 (1998).
[9] B. Fischer, M. Kramer, and Th. Enk, Plasma Phys. Controlled Fusion **36**, 2003 (1994).
[10] I. V. Kamenski and G. G. Borg, Phys. Plasmas **3**, 4396 (1996).
[11] I. V. Kamenski and G. G. Borg, Comput. Phys. Commun. **113**, 1 (1998).
[12] S. Cho and J. Kwak, Phys. Plasmas **4**, 4167 (1997).
[13] Y. Mouzouris and J. E. Scharer, IEEE Trans. Plasma Sci. **24**, 152 (1996).
[14] National Technical Information Center Service Document No. DE85004960, edited by B. D. McVey (''ICRF antenna coupling theory for a cylindrically stratified plasma,'' Report PFC RR-84-13, Plasma Fusion Center, MIT, 1984.) Copies may be ordered from the National Technical Information Center, Springfield, VA 22161.
[15] L. A. Berry and J. C. Whitson (private communication, 1996).
[16] T. H. Stix, *Waves in Plasmas* (American Institute of Physics, New York, 1992).
[17] F. F. Chen, Plasma Phys. Controlled Fusion **33**, 339 (1991).
[18] K. P. Shamrai, V. P. Pavlenko, and V. B. Taranov, Plasma Phys. Controlled Fusion **39**, 505 (1997).
[19] G. G. Borg and R. W. Boswell, Phys. Plasmas **5**, 564 (1998).
[20] K. P. Shamrai and V. B. Taranov, Plasma Sources Sci. Technol. **5**, 474 (1996).
[21] A. R. Ellingboe, R. W. Boswell, J. P. Booth, and N. Sadeghi, Phys. Plasmas **2**, 1807 (1995).
[22] A. W. Degeling, C. O. Jung, R. W. Boswell, and A. R. Ellingboe, Phys. Plasmas **3**, 2788 (1996).
[23] I. D. Sudit and F. F. Chen, Plasma Sources Sci. Technol. **5**, 43 (1996).
[24] I. S. Duff and J. A. Scott, ACM Trans. Math. Softw. **22**, 30 (1996).
[25] P. L. Bhatnagar, E. P. Gross, and M. Krook, Phys. Rev. **94**, 511 (1954).
[26] M. N. O. Sadiku, *Numerical Techniques in Electromagnetics* (CRC Press, Boca Raton, 1992).
[27] B. D. Fried and S. D. Conte, *The Plasma Dispersion Function* (Academic, New York, 1961).
[28] X. Guo and J. Scharer (private communication, 1998).